IOP Publishing Phys. Med. Biol. 63 (2018) 035042 (14pp) https://doi.org/10.1088/1361-6560/aaa71b

Physics in Medicine & Biology

IPEM Institute of Physics and Engineering in Medicine

CrossMark

RECEIVED
13 September 2017

REVISED
26 December 2017

ACCEPTED FOR PUBLICATION
12 January 2018

PUBLISHED
6 February 2018

PAPER

A PET reconstruction formulation that enforces non-negativity in projection space for bias reduction in Y-90 imaging

Hongki Lim[1,2], **Yuni K Dewaraja**[2] and **Jeffrey A Fessler**[1]

[1] Department of Electrical Engineering and Computer Science, University of Michigan, Ann Arbor, MI 48109, United States of America
[2] Department of Radiology, University of Michigan, Ann Arbor, MI 48109, United States of America

E-mail: hongki@umich.edu, yuni@med.umich.edu and fessler@umich.edu

Keywords: PET image reconstruction, bias reduction, Yttrium-90, quantification, radioembolization

Abstract

Most existing PET image reconstruction methods impose a nonnegativity constraint in the image domain that is natural physically, but can lead to biased reconstructions. This bias is particularly problematic for Y-90 PET because of the low probability positron production and high random coincidence fraction. This paper investigates a new PET reconstruction formulation that enforces nonnegativity of the projections instead of the voxel values. This formulation allows some negative voxel values, thereby potentially reducing bias. Unlike the previously reported NEG-ML approach that modifies the Poisson log-likelihood to allow negative values, the new formulation retains the classical Poisson statistical model. To relax the non-negativity constraint embedded in the standard methods for PET reconstruction, we used an alternating direction method of multipliers (ADMM). Because choice of ADMM parameters can greatly influence convergence rate, we applied an automatic parameter selection method to improve the convergence speed. We investigated the methods using lung to liver slices of XCAT phantom. We simulated low true coincidence count-rates with high random fractions corresponding to the typical values from patient imaging in Y-90 microsphere radioembolization. We compared our new methods with standard reconstruction algorithms and NEG-ML and a regularized version thereof. Both our new method and NEG-ML allow more accurate quantification in all volumes of interest while yielding lower noise than the standard method. The performance of NEG-ML can degrade when its user-defined parameter is tuned poorly, while the proposed algorithm is robust to any count level without requiring parameter tuning.

1. Introduction

Interest in quantitative imaging of Y-90 is growing because transarterial radioembolization (RE) with Y-90 loaded microspheres is a promising and minimally invasive treatment that is FDA approved for unresectable primary and metastatic liver tumors. These cancers are a leading cause of cancer mortality and morbidity. Radioembolization is a therapy that irradiates liver tumors with radioactive microspheres administered through a microcatheter placed in the hepatic arterial vasculature. Radioembolization is based on the principle that healthy liver and tumor are mainly vascularized by the portal vein and the hepatic artery respectively (Pasciak *et al* 2016). As a result, radioactive microspheres are preferentially located in the lesions after they are administered via the hepatic artery.

Accurate quantitative Y-90 imaging based dosimetry is important for establishing absorbed dose versus outcome relationships for developing future treatment planning strategies in radioembolization. Additionally, accurately assessing the microsphere distribution is important for finding unexpected extra-hepatic deposition. However, imaging of Y-90 is complex as it is an almost pure beta emitter, with no associated gamma-rays. Y-90 imaging involves SPECT via bremsstrahlung photons or PET via very low probability ($\sim 3.2 \times 10^{-5}$) positrons in the presence of increased singles events from bremsstrahlung photons and gammas from natural radioactivity in Lu-based crystals used in some PET systems. Due to these attributes of Y-90, positive bias in cold regions and underestimation in regions of interest are reported in many Y-90 PET papers (Pasciak *et al* 2014, Carlier *et al* 2015

© 2018 Institute of Physics and Engineering in Medicine

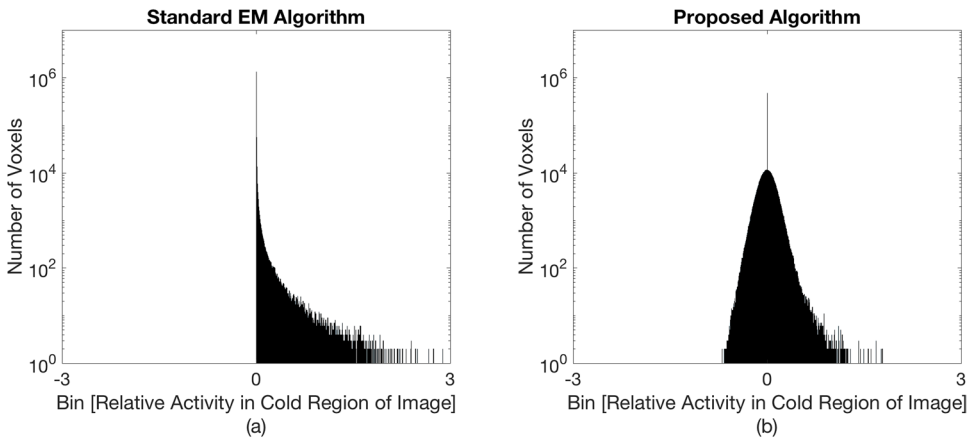

Figure 1. Reconstruction results when simulating realistic conditions of low count rates: (a) a histogram showing how the standard reconstruction algorithm (EM) can have a positive bias in the cold regions in the setting of lower count-rates. Cold region refers to the outside of the liver where the true image has no counts. An example slice of the true image is shown in figure 2. (b) A histogram illustrating how the proposed method avoids the positive bias by allowing negative values.

and Strydhorst *et al* 2016). Those reports conclude that the bias is introduced by the current standard PET reconstruction algorithms that enforce a nonnegativity constraint in the image domain. Figure 1(a) illustrates how the standard expectation maximization (EM) image reconstruction algorithm generates positive bias in a low count-rate setting.

Recent studies have demonstrated improved Y-90 PET imaging with time-of-flight (TOF) information and acquisitions that allow for randoms smoothing (Willowson *et al* 2015). However, quantitative imaging under the low count-rates typical for Y-90 PET remains challenging. Though not specific to Y-90, others have previously proposed reconstruction algorithms to mitigate the bias issue in low-statistics PET/SPECT. AB-EMML (Byrne 1998) was devised for the deblurring problem, however, (Erlandsson *et al* 2000) used this method for low count-rate scans because AB-EMML allows negative values when the lower boundary is set below 0. NEG-ML (Nuyts *et al* 2000) was introduced for non-attenuation corrected PET, but it was also shown to be effective to reduce the bias (Grezes-Besset *et al* 2007). A modified version of NEG-ML was introduced in Nuyts *et al* (2011) that includes two factors giving more flexibility for Gaussian distribution switching point and allowing faster convergence.

Both the AB-EMML and the NEG-ML approaches use modifications of the log-likelihood for Poisson data. Because ML estimation (based on the correct statistical model) is known to be asymptotically efficient (lowest possible variance), modifying the log-likelihood may affect image noise properties and the modifications require additional parameters to tune. Our objective is similar to these previous works, namely reducing the bias observed in low statistics PET, especially for Y-90 PET. However, our proposed algorithm is distinct in avoiding modifying or approximating the Poisson log-likelihood used in the data fit term. We propose a method to relax the conventional image-domain nonnegativity constraint by instead imposing a positivity constraint on the predicted measurement mean. We adopt ADMM to perform reconstruction that enforces this constraint. Figure 1(b) demonstrates how the proposed method overcomes the positive bias evident in figure 1(a).

Section 2 presents the formulation of our proposed PET reconstruction algorithm and reviews how the update in various algorithms changes when the cost function includes a regularization term. Section 3 explains the simulation method in the setting of Y-90 radioembolization and the evaluation metrics used for the quantification assessment. Section 4 investigates how the various reconstruction methods work when the number of projection angles replicates 3D and fully 3D PET and examines the impact of parameter selection. Section 5 discusses the strengths and limitations of each method.

2. Methods

This section reviews the typical problem formulation in emission tomography. Then we explain how we formulate a new constrained reconstruction approach and we present various methods that incorporate regularization.

2.1. Emission tomography

The goal in emission tomography is to find an emission distribution $\boldsymbol{x} = (x_1, ..., x_{n_p})$ (counts) from a realization $\boldsymbol{y} = (y_1, ..., y_{n_d})$ (counts) of the projection measurement vector $\boldsymbol{Y} = (Y_1, ..., Y_{n_d})$, where n_p is the number of voxels of unknown functional image and n_d is the number of rays. Emission measurement $\boldsymbol{Y}$ follows Poisson statistical model as follows:

$$Y_i \sim \text{Poisson}\{\bar{y}_i(\boldsymbol{x}_{\text{true}})\}, \quad i = 1, ..., n_d, \tag{1}$$

where $\boldsymbol{x}_{\text{true}}$ is true unknown value that we want to estimate and $\bar{y}_i(\boldsymbol{x})$ (counts) is the measurement mean:

$$\bar{y}_i(\boldsymbol{x}) = \text{E}[Y_i] = \sum_{j=1}^{n_p} a_{ij}x_j + \bar{r}_i = [\boldsymbol{Ax}]_i + \bar{r}_i. \tag{2}$$

The matrix $\boldsymbol{A}$ denotes the system model, incorporating factors such as attenuation coefficients, where a_{ij} (unitless) is the probability that an emission from the jth voxel is recorded in the ith ray. $\bar{r}_i$ denotes the mean background events such as scatter and random coincidence for the ith ray. The maximum likelihood (ML) estimate $\hat{\boldsymbol{x}}$ of $\boldsymbol{x}_{\text{true}}$ minimizes the Poisson negative log-likelihood $f(\boldsymbol{x})$:

$$f(\boldsymbol{x}) \stackrel{c}{=} \sum_{i=1}^{n_d} \text{q}_i([\boldsymbol{Ax}]_i), \tag{3}$$

where

$$\text{q}_i(t) = \begin{cases} t + \bar{r}_i - y_i \log(t + \bar{r}_i), & y_i > 0, \quad t + \bar{r}_i > 0 \\ t + \bar{r}_i, & y_i = 0 \\ \infty, & y_i > 0, \quad t + \bar{r}_i \leqslant 0. \end{cases} \tag{4}$$

Here, $\stackrel{c}{=}$ indicates that we exclude constants independent of $\boldsymbol{x}$. When $\boldsymbol{x} \geqslant 0$, $f(\boldsymbol{x})$ matches with the original Poisson negative log-likelihood function. The following formulation summarizes the conventional emission tomography problem with a nonnegativity constraint:

$$\hat{\boldsymbol{x}} = \underset{\boldsymbol{x}}{\text{argmin}} f(\boldsymbol{x}) \tag{5}$$

$$\text{subject to } \boldsymbol{x} \geqslant 0. \tag{6}$$

The typical approach for solving this formulation is to find a surrogate function $Q(\boldsymbol{x})$ of the log-likelihood that is easier to monotonically decrease than $f(\boldsymbol{x})$. The following subsection briefly reviews a reconstruction algorithm based on this formulation.

2.1.1. SPS algorithm

The separable paraboloidal surrogate (SPS) algorithm for (5) uses a quadratic majorizer for $f(\boldsymbol{x})$ and updates x_j by minimizing the separable surrogate function $Q_{\text{SPS},j}$ using Newton's method:

$$x_j^{(n+1)} = \left[x_j^{(n)} - \frac{\frac{\partial Q_{\text{SPS},j}(x_j;\boldsymbol{x}^{(n)})}{\partial x_j}\Big|_{x_j = x_j^{(n)}}}{\frac{\partial^2 Q_{\text{SPS},j}(x_j;\boldsymbol{x}^{(n)})}{\partial x_j^2}} \right]_+, \tag{7}$$

where $[.]_+$ enforces the voxel nonnegativity constraint and (see Sotthivirat and Fessler (2002)):

$$Q_{\text{SPS},j}(x_j;\boldsymbol{x}^{(n)}) \stackrel{c}{=} \sum_{i=1}^{n_d} \left(a_{ij}(1 - \frac{y_i}{\bar{y}_i^{(n)}})(x_j - x_j^{(n)}) + \frac{\breve{c}_i^{(n)} a_i}{2}(x_j - x_j^{(n)})^2 \right) \tag{8}$$

$$\frac{\partial Q_{\text{SPS},j}(x_j;\boldsymbol{x}^{(n)})}{\partial x_j}\Big|_{x_j = x_j^{(n)}} = \sum_{i=1}^{n_d} (1 - \frac{y_i}{\bar{y}_i^{(n)}}) a_{ij} = \frac{\partial f(\boldsymbol{x}^{(n)})}{\partial x_j} \tag{9}$$

$$\frac{\partial^2 Q_{\text{SPS},j}(x_j;\boldsymbol{x}^{(n)})}{\partial x_j^2} = \sum_{i=1}^{n_d} \breve{c}_i^{(n)} a_{ij} a_i \tag{10}$$

$$\breve{c}_i^{(n)} = \frac{2}{(l_i^{(n)})^2} \left[l_i^{(n)} \dot{\text{q}}_i(l_i^{(n)}) + \text{q}_i(0) - \text{q}_i(l_i^{(n)}) \right]. \tag{11}$$

$\bar{y}_i^{(n)}$ denotes $\bar{y}_i(\boldsymbol{x}^{(n)})$ and $\boldsymbol{x}^{(n)}$ is the estimated $\boldsymbol{x}$ at the nth iteration. $l_i^{(n)}$ and a_i denote $[\boldsymbol{Ax}^{(n)}]_i$ and $\sum_{j=1}^{n_p} a_{ij}$ respectively. Considerations on the condition of $\bar{\boldsymbol{r}}$ ($\bar{r}_i > 0$), choosing the optimal curvature $\breve{c}_i^{(n)}$ and deriving separable surrogate function are shown in Fessler and Erdogan (1998) and Erdogan and Fessler (1999). The matrix-vector form of (7)–(10) is

$$\boldsymbol{x}^{(n+1)} = \left[\boldsymbol{x}^{(n)} - \left(\boldsymbol{D}^{(n)}\right)^{-1} \nabla f(\boldsymbol{x}^n) \right]_+, \tag{12}$$

where $\boldsymbol{D}^{(n)}$ is a diagonal matrix with diagonal elements $A^T\,\mathbf{diag}\{\breve{c}_i^{(n)}\}A\mathbf{1}$ where $\mathbf{1}$ denotes the vector of ones of length n_p and ∇f is in (9).

2.1.2. NEG-ML algorithm

The approach of NEG-ML algorithm is similar to the SPS algorithm in that it uses a quadratic majorizer of the data fit term. However, NEG-ML minimizes a modified data fit term $f_{\mathrm{NEG-ML}}(\boldsymbol{x})$ where the Poisson distribution is replaced by Gaussian distribution when the estimated measurement is below than the parameter ψ:

$$f_{\mathrm{NEG-ML}}(\boldsymbol{x}) \overset{c}{=} \sum_{i=1}^{n_d} \tilde{\mathrm{q}}_i([\boldsymbol{Ax}]_i), \tag{13}$$

where

$$\tilde{\mathrm{q}}_i(t) = \begin{cases} t + \bar{r}_i - y_i \log(t + \bar{r}_i), & t + \bar{r}_i \geqslant \psi \\ \frac{(y_i - t - \bar{r}_i)^2}{2\psi} - y_i \log \psi + \psi - \frac{(y_i - \psi)^2}{2\psi}, & t + \bar{r}_i < \psi. \end{cases} \tag{14}$$

Minimizing a separable surrogate function of (14) using Newton's method leads to the following NEG-ML iteration:

$$x_j^{(n+1)} = x_j^{(n)} - \frac{\sum_{i=1}^{n_d} a_{ij} \frac{\bar{y}_i^{(n)} - y_i}{\max(\psi, \bar{y}_i^{(n)})}}{\sum_{i=1}^{n_d} a_{ij} \frac{a_i}{\max(\psi, \bar{y}_i^{(n)})}}. \tag{15}$$

Derivation details are shown in Van Slambrouck *et al* (2015).

2.2. Proposed formulation

As shown in previous section, the standard methods for reconstructing emission images are based on nonnegativity constraint in image domain: $\boldsymbol{x} \geqslant 0$. This is a natural constraint as the activity distribution cannot have negative values physically. However, this constraint can cause positive biases in regions of low or no activity, especially when the measured counts are low and the background events $\bar{r}_i$ are dominant.

To loosen the nonnegativity constraint in hope of reducing the positive bias, we propose to allow negative values in image domain while keeping positivity in projection space. We propose the following formulation:

$$\hat{\boldsymbol{x}} = \underset{\boldsymbol{x}}{\operatorname{argmin}}\, f(\boldsymbol{x}), \quad \text{subject to } \boldsymbol{Ax} + \bar{\boldsymbol{r}} > 0. \tag{16}$$

The constraint $\boldsymbol{Ax} + \bar{\boldsymbol{r}} > 0$ is reasonable because likelihood function $f(\boldsymbol{x})$ includes $\log(\boldsymbol{Ax} + \bar{\boldsymbol{r}})$ and the argument of a logarithm should be positive. We rewrite this optimization problem in the following unconstrained composite formulation:

$$\hat{\boldsymbol{x}} = \underset{\boldsymbol{x} \in \mathbb{R}^{n_p}}{\operatorname{argmin}}\, f(\boldsymbol{x}) + g(\boldsymbol{Ax} + \bar{\boldsymbol{r}}), \tag{17}$$

where

$$g(\eta_i) = \begin{cases} \infty, & y_i > 0,\ \eta_i < 0 \\ 0, & \text{else} \end{cases} \tag{18}$$

$$g(\boldsymbol{\eta}) = \sum_{i=1}^{n_d} g_i(\eta_i) \tag{19}$$

for a vector argument $\boldsymbol{\eta} \in \mathbb{R}^{n_d}$. To perform this minimization, we introduce an auxiliary variable $\boldsymbol{v}$ leading to the following equality constrained optimization problem:

$$\hat{\boldsymbol{x}} = \underset{\boldsymbol{x} \in \mathbb{R}^{n_p}}{\operatorname{argmin}} \min_{\boldsymbol{v} \in \mathbb{R}^{n_d}} \mathbf{1}^T(\boldsymbol{v} + \bar{\boldsymbol{r}}) - \boldsymbol{y}^T \log(\boldsymbol{v} + \bar{\boldsymbol{r}}) + g(\boldsymbol{v} + \bar{\boldsymbol{r}}) \tag{20}$$

$$\text{subject to } \boldsymbol{v} = \boldsymbol{Ax}. \tag{21}$$

We form an augmented Lagrangian based on that formulation:

$$\Psi(\boldsymbol{x}, \boldsymbol{v}, \boldsymbol{\lambda}) = \mathbf{1}^T(\boldsymbol{v} + \bar{\boldsymbol{r}}) - \boldsymbol{y}^T \log(\boldsymbol{v} + \bar{\boldsymbol{r}}) + g(\boldsymbol{v} + \bar{\boldsymbol{r}}) + \boldsymbol{\lambda}^T(\boldsymbol{Ax} - \boldsymbol{v}) + \frac{\rho}{2}||\boldsymbol{Ax} - \boldsymbol{v}||_2^2, \tag{22}$$

where $\boldsymbol{\lambda}$ is a dual variable and $\rho > 0$ is called the penalty parameter and it affects the convergence rate but not the final minimum. Letting $\boldsymbol{d} = \boldsymbol{Ax} - \boldsymbol{v}$, $\boldsymbol{u} = \frac{\boldsymbol{\lambda}}{\rho}$, we rewrite $\boldsymbol{\lambda}^T(\boldsymbol{Ax} - \boldsymbol{v}) + \frac{\rho}{2}||\boldsymbol{Ax} - \boldsymbol{v}||_2^2$ in a simpler form:

$$\begin{aligned}\boldsymbol{\lambda}^T(\boldsymbol{A}\boldsymbol{x}-\boldsymbol{v})+\frac{\rho}{2}||\boldsymbol{A}\boldsymbol{x}-\boldsymbol{v}||_2^2 &= \boldsymbol{\lambda}^T\boldsymbol{d}+\frac{\rho}{2}||\boldsymbol{d}||_2^2\\ &= \frac{\rho}{2}||\boldsymbol{d}+\frac{\boldsymbol{\lambda}}{\rho}||_2^2-\frac{1}{2\rho}||\boldsymbol{\lambda}||_2^2\\ &= \frac{\rho}{2}||\boldsymbol{A}\boldsymbol{x}-\boldsymbol{v}+\boldsymbol{u}||_2^2-\frac{\rho}{2}||\boldsymbol{u}||_2^2.\end{aligned} \tag{23}$$

Then the augmented Lagrangian becomes the following equivalent expression:

$$\Psi(\boldsymbol{x},\boldsymbol{v},\boldsymbol{u})=\boldsymbol{1}^T(\boldsymbol{v}+\bar{\boldsymbol{r}})-\boldsymbol{y}^T\log(\boldsymbol{v}+\bar{\boldsymbol{r}})+g(\boldsymbol{v}+\bar{\boldsymbol{r}})+\frac{\rho}{2}||\boldsymbol{A}\boldsymbol{x}-\boldsymbol{v}+\boldsymbol{u}||_2^2-\frac{\rho}{2}||\boldsymbol{u}||_2^2. \tag{24}$$

Finding the saddle point of (24) is equivalent to solving the problem (20) and (21):

$$\hat{\boldsymbol{x}}=\underset{\boldsymbol{x}\in\mathbb{R}^{np}}{\operatorname{argmin}}\ \min_{\boldsymbol{v}\in\mathbb{R}^{n_d}}\ \max_{\boldsymbol{u}\in\mathbb{R}^{n_d}}\Psi(\boldsymbol{x},\boldsymbol{v},\boldsymbol{u}). \tag{25}$$

ADMM (Boyd *et al* 2010) approaches the saddle point of the augmented Lagrangian function by updating variables $\boldsymbol{x}, \boldsymbol{v}, \boldsymbol{u}$ in the following sequential way:

$$\boldsymbol{x}^{(n+1)}=\underset{\boldsymbol{x}}{\operatorname{argmin}}\ \frac{\rho}{2}||\boldsymbol{A}\boldsymbol{x}-\boldsymbol{v}^{(n)}+\boldsymbol{u}^{(n)}||_2^2 \tag{26}$$

$$\boldsymbol{v}^{(n+1)}=\underset{\boldsymbol{v}}{\operatorname{argmin}}\left(\boldsymbol{1}^T(\boldsymbol{v}+\bar{\boldsymbol{r}})-\boldsymbol{y}^T\log(\boldsymbol{v}+\bar{\boldsymbol{r}})+g(\boldsymbol{v}+\bar{\boldsymbol{r}})+\frac{\rho}{2}||\boldsymbol{A}\boldsymbol{x}^{(n+1)}-\boldsymbol{v}+\boldsymbol{u}^{(n)}||_2^2\right) \tag{27}$$

$$\boldsymbol{u}^{(n+1)}=\boldsymbol{u}^{(n)}+(\boldsymbol{A}\boldsymbol{x}^{(n+1)}-\boldsymbol{v}^{(n+1)}). \tag{28}$$

In the implementation, we initialize $\boldsymbol{v}^{(0)}=\boldsymbol{A}\boldsymbol{x}^{(0)}$ and $\boldsymbol{u}^{(0)}=\boldsymbol{0}$. ADMM is an extension of the method of multipliers algorithm where (26) and (27) can be viewed as a finding primal optimal points in a sequential fashion and (28) as finding a dual optimal point.

2.2.1. $\boldsymbol{x}$-update

An established minimization method to solve the quadratic problem in (26) is the conjugate gradient (CG) algorithm. In our implementation, we used just one iteration of CG, which is equivalent to one iteration of steepest descent (SD):

$$\boldsymbol{g}^{(n)}=\rho\boldsymbol{A}^T(\boldsymbol{A}\boldsymbol{x}^{(n)}-\boldsymbol{v}^{(n)}+\boldsymbol{u}^{(n)}) \tag{29}$$

$$\zeta_n=\frac{||\boldsymbol{g}^{(n)}||^2}{\rho||\boldsymbol{A}\boldsymbol{g}^{(n)}||^2} \tag{30}$$

$$\boldsymbol{x}^{(n+1)}=\boldsymbol{x}^{(n)}-\zeta_n\boldsymbol{g}^{(n)}. \tag{31}$$

2.2.2. $\boldsymbol{v}$-update

For the $\boldsymbol{v}$-update, we first find the minimizer $\hat{\boldsymbol{v}}$ of (27) excluding the $g(\boldsymbol{v}+\bar{\boldsymbol{r}})$ term using its separability:

$$\boldsymbol{1}^T(\boldsymbol{v}+\bar{\boldsymbol{r}})-\boldsymbol{y}^T\log(\boldsymbol{v}+\bar{\boldsymbol{r}})+\frac{\rho}{2}||\boldsymbol{A}\boldsymbol{x}^{(n+1)}-\boldsymbol{v}+\boldsymbol{u}^{(n)}||_2^2 \tag{32}$$

$$=\sum_{i=1}^{n_d}\left(v_i+\bar{r}_i-y_i\log(v_i+\bar{r}_i)+\frac{\rho}{2}([\boldsymbol{A}\boldsymbol{x}^{(n+1)}]_i-v_i+u_i^{(n)})^2\right)=\sum_{i=1}^{n_d}k(v_i). \tag{33}$$

Zeroing the derivative of $k(v_i)$ and finding the root leads to the minimizer:

$$\hat{v}_i=\begin{cases}[\boldsymbol{A}\boldsymbol{x}^{(n+1)}]_i+u_i^{(n)}-\frac{1}{\rho}, & y_i=0\\ \sqrt{\beta^2+\gamma}-\beta, & y_i>0,\ \beta<0\\ \frac{\nu}{\sqrt{\beta^2+\gamma}+\beta}, & y_i>0,\ \beta\geqslant 0,\end{cases} \tag{34}$$

where

$$\beta=\frac{1}{2}(\frac{1}{\rho}+\bar{r}_i-u_i^{(n)}-[\boldsymbol{A}\boldsymbol{x}^{(n+1)}]_i) \tag{35}$$

$$\gamma=\bar{r}_i(u_i^{(n)}+[\boldsymbol{A}\boldsymbol{x}^{(n+1)}]_i)-\frac{\bar{r}_i-y_i}{\rho}. \tag{36}$$

Lastly, we consider $g(\boldsymbol{v}+\bar{\boldsymbol{r}})$ constraint, leading to the final $\boldsymbol{v}$ update:

$$v_i^{(n+1)} = [\hat{v}_i + \bar{r}_i]_+ - \bar{r}_i. \tag{37}$$

Note that both (35) and (29) require computing $\boldsymbol{A}\boldsymbol{x}^{(n)}$ so an efficient implementation saves this product so only one new forward project per iteration is needed.

2.2.3. Parameter ρ selection

Manually selecting parameter ρ of ADMM algorithm often leads to slow convergence. Boyd *et al* (2010) introduced an approach to adaptively tune the parameter by comparing the primal and dual residual. We followed the comparison criteria choice in Boyd *et al* (2010).

2.3. Regularization

We also derived and implemented algorithms for minimizing cost functions that include a regularization term $\mathsf{R}(\boldsymbol{x})$ to penalize the image roughness and control noise:

$$\mathsf{R}(\boldsymbol{x}) = \sum_{k=1}^{K} \psi_k([\boldsymbol{C}\boldsymbol{x}]_k), \tag{38}$$

where $\boldsymbol{C}$ is a $K \times n_p$ finite differencing matrix. It is preferable for potential function ψ_k to include continuity, symmetry, and positivity (Li 1998). There are several available choices for potential function and each option has its own advantage/disadvantage. For the results in this paper, we used a simple quadratic potential function:

$$\psi(t) = \frac{t^2}{2}. \tag{39}$$

We designed $\boldsymbol{C}$ to generate finite differences in 3D. Including a regularization term in the cost function for emission tomography leads to the following minimization problems:

$$\hat{\boldsymbol{x}} = \underset{\boldsymbol{x}}{\operatorname{argmin}}\, f(\boldsymbol{x}) + \beta \mathsf{R}(\boldsymbol{x}) \tag{40}$$

$$\text{subject to } \boldsymbol{A}\boldsymbol{x} + \bar{\boldsymbol{r}} \geqslant 0 (\text{ proposed}) \tag{41}$$

$$\text{or } \boldsymbol{x} \geqslant 0 (\text{conventional}), \tag{42}$$

where β is a parameter specifying how much we want to penalize the roughness. The following subsections briefly list solutions to (40)–(42) with the various approaches.

2.3.1. Regularized SPS algorithm

Finding optimal $\boldsymbol{x}$ for (40) with the standard constraint $\boldsymbol{x} \geqslant 0$ is an extension of the SPS algorithm. We used the standard separable surrogate function $Q_{\mathsf{R},j}$ for $\beta\mathsf{R}(\boldsymbol{x})$ (De Pierro 1995):

$$Q_{\mathsf{R},j}(x_j; x^{(n)}) \stackrel{c}{=} \beta \sum_{k=1}^{K} \left(c_{kj}[\boldsymbol{C}\boldsymbol{x}^{(n)}]_k (x_j - x_j^{(n)}) + \frac{1}{2}|c_{kj}| c_k (x_j - x_j^{(n)})^2 \right), \tag{43}$$

$$x_j^{(n+1)} = \left[x_j^{(n)} - \frac{\frac{\partial Q_{\mathrm{SPS},j}(x_j;\boldsymbol{x}^{(n)})}{\partial x_j}\Big|_{x_j = x_j^{(n)}} + \frac{\partial Q_{\mathsf{R},j}(x_j;\boldsymbol{x}^{(n)})}{\partial x_j}\Big|_{x_j = x_j^{(n)}}}{\frac{\partial^2 Q_{\mathrm{SPS},j}(x_j;\boldsymbol{x}^{(n)})}{\partial x_j^2} + \frac{\partial^2 Q_{\mathsf{R},j}(x_j;\boldsymbol{x}^{(n)})}{\partial x_j^2}} \right]_+ \tag{44}$$

$$= \left[x_j^{(n)} - \frac{\sum_{i=1}^{n_d} \left(1 - \frac{y_i}{\bar{y}_i^{(n)}}\right) a_{ij} + \beta \sum_{k=1}^{K} c_{kj} [\boldsymbol{C}\boldsymbol{x}^{(n)}]_k}{\sum_{i=1}^{n_d} \breve{c}_i^{(n)} a_{ij} a_i + \beta \sum_{k=1}^{K} |c_{kj}| c_k} \right]_+, \tag{45}$$

where c_k denotes $\sum_{j=1}^{n_p} |c_{kj}|$.

2.3.2. Regularized NEG-ML

NEG-ML also use the quadratic majorizer of the modified likelihood function; therefore, the scheme for $\boldsymbol{x}$-update of regularized NEG-ML is analogous to regularized SPS algorithm:

$$x_j^{(n+1)} = x_j^{(n)} - \frac{\sum_{i=1}^{n_d} a_{ij} \frac{\bar{y}_i^{(n)} - y_i}{\max(\psi, \bar{y}_i^{(n)})} + \beta \sum_{k=1}^{K} c_{kj} [\boldsymbol{C}\boldsymbol{x}^{(n)}]_k}{\sum_{i=1}^{n_d} a_{ij} \frac{a_i}{\max(\psi, \bar{y}_i^{(n)})} + \beta \sum_{k=1}^{K} |c_{kj}| c_k}, \tag{46}$$

Table 1. Administered activity and randoms fractions for two patients treated at our clinic with Y-90 radioembolization.

	Patient A	Patient B
Y-90 Injection(GBq)	3.9	0.9
True prompts	675 498	96 890
Random prompts	3275 353	1692 504
Total prompts	3950 851	1789 394
Random fraction[a] (%)	83	95

[a] Random Fraction = (Random prompts / Total prompts) × 100.

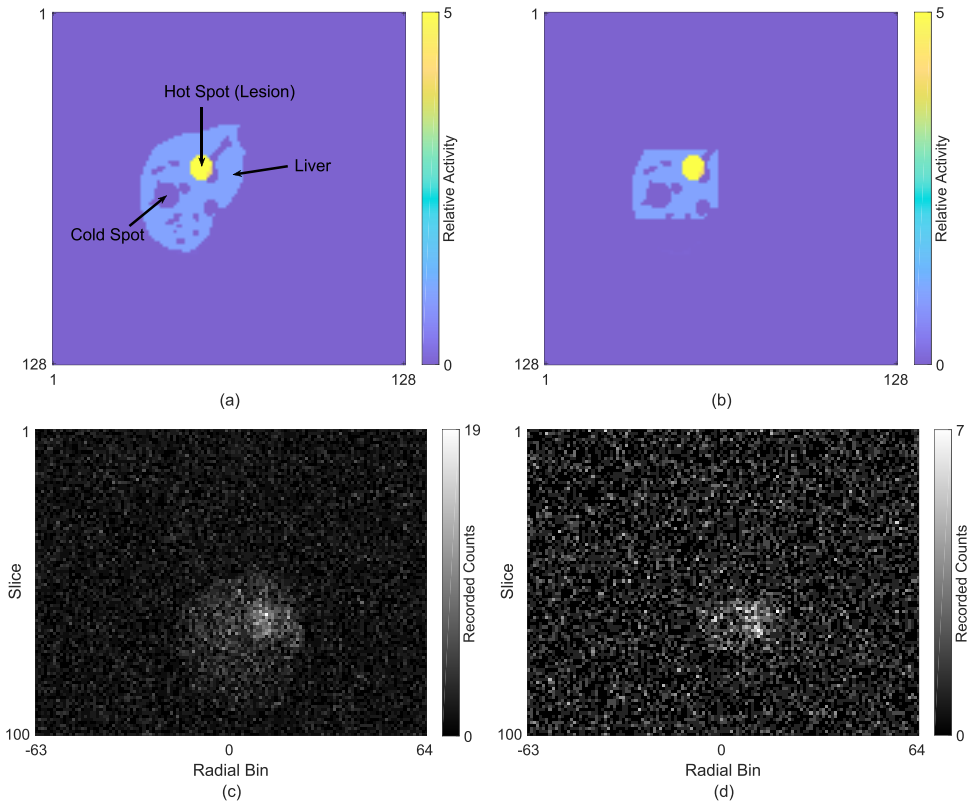

Figure 2. True image and the corresponding projection: (a), (c) and (b), (d) are slices of true image and projection views at one angle simulating the conditions of patient A and B data respectively. Activity concentration ratio between healthy liver and hot spot (lesion) is 1:5 to simulate the typical uptake ratio.

where ψ is a parameter indicating the likelihood function switching point between the Poisson distribution and the Gaussian distribution. We set the convergence-related step-size as 1 in our implementation.

2.3.3. *Proposed algorithm with regularization*

Including $\mathsf{R}(\boldsymbol{x})$ in the cost function requires only modifications to (24) and (29) and (30) for the $\boldsymbol{x}$-update in section 2.2.1:

$$\Psi(\boldsymbol{x},\boldsymbol{v},\boldsymbol{u}) = \mathbf{1}^T(\boldsymbol{v}+\bar{\boldsymbol{r}}) - \boldsymbol{y}^T\log(\boldsymbol{v}+\bar{\boldsymbol{r}}) + \beta\mathsf{R}(\boldsymbol{x}) + g(\boldsymbol{v}+\bar{\boldsymbol{r}}) + \frac{\rho}{2}||\boldsymbol{A}\boldsymbol{x}-\boldsymbol{v}+\boldsymbol{u}||_2^2 - \frac{\rho}{2}||\boldsymbol{u}||_2^2 \tag{47}$$

$$\boldsymbol{g}^{(n)} = \rho\boldsymbol{A}^T(\boldsymbol{A}\boldsymbol{x}^{(n)} - \boldsymbol{v}^{(n)} + \boldsymbol{u}^{(n)}) + \beta\boldsymbol{C}^T\boldsymbol{C}\boldsymbol{x}^{(n)} \tag{48}$$

$$\zeta_n = \frac{||\boldsymbol{g}^{(n)}||^2}{\rho||\boldsymbol{A}\boldsymbol{g}^{(n)}||^2 + \beta||\boldsymbol{C}\boldsymbol{g}^{(n)}||^2}. \tag{49}$$

3. Experimental method

This section describes the simulation setting and what evaluation metrics are used to assess the efficacy of each algorithm.

3.1. Simulation

3.1.1. True image

We simulated extremely low-count scans, typical for Y-90 PET following radioembolization, with the extended cardiac-torso (XCAT) (figure 2). We set the image size to 128 × 128 × 100 with a voxel size 4.0 × 4.0 × 4.0 (mm^3) and chose 100 slices ranging from lung to liver. The activity concentration ratio between healthy liver and a 42 ml lesion was 1:5 to simulate a typical uptake ratio. We also placed a 42 ml zero valued cold spot in the liver. In one case activity was assigned to the entire liver, while in the other case only to part of the liver as lobar or segmental treatment is common. Activity assigned to the lungs simulated a lung shunt of 5%. The rest of the phantom is 'cold'.

3.1.2. Projection

Our experiment uses the framework of Michigan Image Reconstruction Toolbox (MIRT)[3]. We first set the projection size to 128 × 100 with 168 projection angles and the detector width to 8 mm when specifying the system model. For realistic simulation, we replicate the true and random counts observed in the patient imaging following radioembolization. Table 1 shows the low count conditions that we simulated corresponding to a relatively high Y-90 administration (Patient A) and a relatively low administration (Patient B) for patients treated at our clinic with glass microspheres. We use smaller area of liver (figure 2(b)) in the Patient B case because lower Y-90 administration and consequent lower true counts are usually induced by treatment of smaller region in the liver. Simulated projections are shown in figures 2(c) and (d).

We also investigated increasing the number of projection angles by 10 times (while keeping total counts the same) to emulate fully 3D-PET (TOF) and test how each algorithm would work in the fully 3D-PET setting (Van Slambrouck *et al* 2015). Section 4.2 discusses the results for this case.

3.2. Evaluation metrics

We eroded each volume of interest (VOI) by 2 pixels to exclude resolution effects from the evaluation. We evaluated liver quantification by calculating activity recovery:

$$\text{Activity recovery in liver } (\%) = \frac{\text{Estimated mean counts}}{\text{True mean counts}} \times 100\% \tag{50}$$

$$= \frac{\frac{1}{MJ_{\text{Liver}}} \sum_{m=1}^{M} \sum_{j \in \text{Liver}} \hat{\boldsymbol{x}}_m[j]}{\frac{1}{J_{\text{Liver}}} \sum_{j \in \text{Liver}} \boldsymbol{x}_{\text{true}}[j]} \times 100\%, \tag{51}$$

where M is the number of realizations and J_{Liver} is the number of voxels in the volume of liver. Estimated mean counts is calculated from the multiple realizations. We used 10 realizations in our experiment ($M = 10$). $\hat{\boldsymbol{x}}_m[j]$ indicates the jth voxel value at mth realization and $\boldsymbol{x}_{\text{true}}[j]$ denotes the jth voxel value of true counts.

Quantification in hot and cold spot (where true value of voxel is zero) are evaluated based on contrast recovery[4]:

$$\text{Contrast recovery in hot spot } (\%) = \frac{C_i/C_{\text{BKG}} - 1}{R - 1} \times 100\% \tag{52}$$

$$= \frac{\frac{\frac{1}{MJ_{\text{Hotspot}}} \sum_{m=1}^{M} \sum_{j \in \text{Hotspot}} \hat{\boldsymbol{x}}_m[j]}{\frac{1}{J_{\text{Liver}}} \sum_{j \in \text{Liver}} \boldsymbol{x}_{\text{true}}[j]} - 1}{\frac{\frac{1}{J_{\text{Hotspot}}} \sum_{j \in \text{Hotspot}} \boldsymbol{x}_{\text{true}}[j]}{\frac{1}{J_{\text{Liver}}} \sum_{j \in \text{Liver}} \boldsymbol{x}_{\text{true}}[j]} - 1} \times 100\% \tag{53}$$

$$\text{Contrast recovery in cold spot } (\%) = (1 - \frac{C_i}{C_{\text{BKG}}}) \times 100\% \tag{54}$$

$$= \left(1 - \frac{\frac{1}{MJ_{\text{Coldspot}}} \sum_{m=1}^{M} \sum_{j \in \text{Coldspot}} \hat{\boldsymbol{x}}_m[j]}{\frac{1}{J_{\text{Liver}}} \sum_{j \in \text{Liver}} \boldsymbol{x}_{\text{true}}[j]}\right) \times 100\%. \tag{55}$$

C_i is the mean counts for object i and C_{BKG} is mean background (eroded liver) counts. R is the true lesion-to-normal liver activity concentration ratio. We also study the counts bias the in field of view (FOV):

$$\text{FOV bias } (\%) = \frac{(\text{Total estimated counts} - \text{Total true counts})}{\text{Total true counts}} \times 100\% \tag{56}$$

[3] http://web.eecs.umich.edu/~fessler/code/index.html.

[4] http://nema.org/Standards/Pages/Performance-Measurements-of-Positron-Emission-Tomographs.aspx.

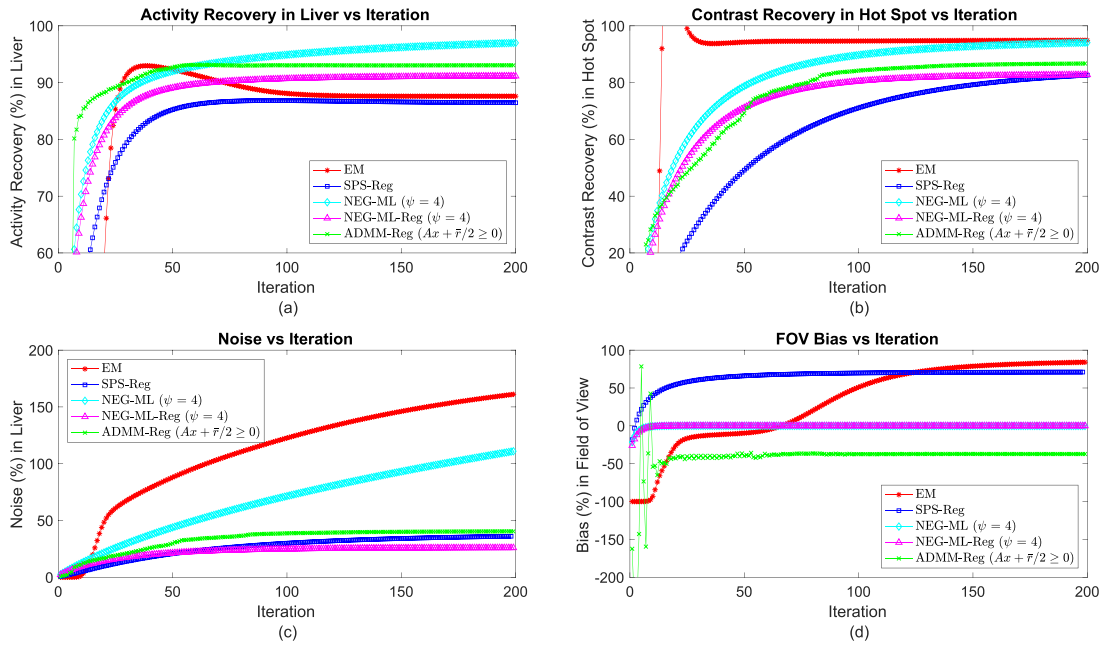

Figure 3. Results from simulating Patient B conditions. Proposed algorithm (green) gives higher contrast and better activity recovery than other regularized algorithms but NEG-ML-Reg (magenta) has lower noise in liver and FOV bias.

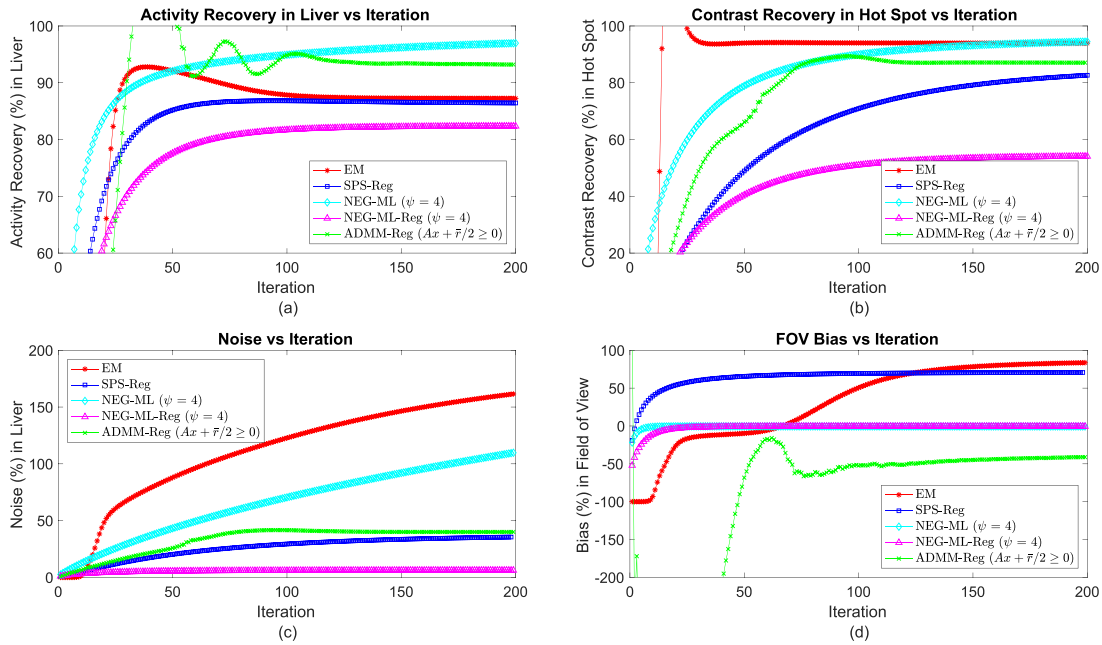

Figure 4. Evaluation result on simulation of fully 3D-PET (number of projection angles is 1680). Proposed algorithm converges to similar point in figure 3, whereas NEG-ML-Reg changes its converged point.

$$= \frac{\left(\frac{1}{M}\sum_{m=1}^{M}\sum_{j=1}^{n_p}\hat{\boldsymbol{x}}_m[j] - \sum_{j=1}^{n_p}\boldsymbol{x}_{\text{true}}[j]\right)}{\sum_{j=1}^{n_p}\boldsymbol{x}_{\text{true}}[j]} \times 100\%. \tag{57}$$

Lastly, we calculate the image ensemble noise across realizations averaged over the liver to evaluate the variability across realizations:

$$\text{Image ensemble noise } (\%) = \frac{\sqrt{\frac{1}{J_{\text{Liver}}}\sum_{j\in\text{Liver}}\left(\frac{1}{M-1}\sum_{m=1}^{M}(\hat{\boldsymbol{x}}_m[j] - \frac{1}{M}\sum_{m'=1}^{M}\hat{\boldsymbol{x}}_{m'}[j])^2\right)}}{\frac{1}{J_{\text{Liver}}}\sum_{j\in\text{Liver}}\boldsymbol{x}_{\text{true}}[j]} \times 100\%, \tag{58}$$

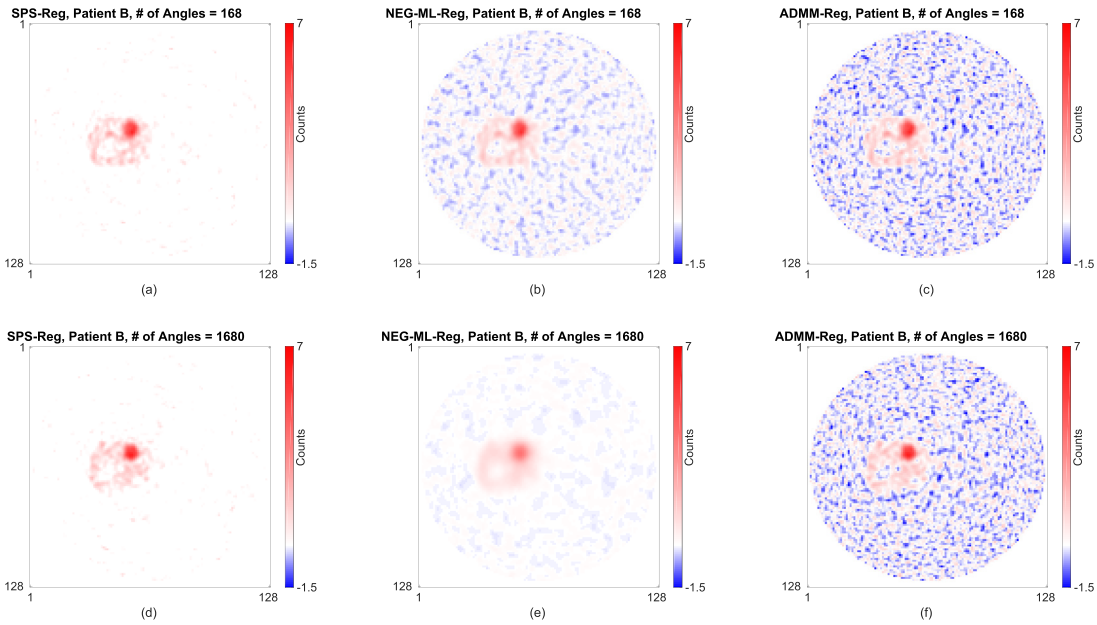

Figure 5. Reconstructed images using regularized SPS, NEG-ML-Reg with $\psi = 4$ and proposed algorithm. True image corresponds to figure 2(b). First row and second row are the results when the number of projection angle is 168 and 1680 respectively. Regularized SPS and proposed algorithm do not change much when the number of angles is increased. However, NEG-ML-Reg ($\psi = 4$) gets blurred.

4. Results

We compare the proposed method with regularization (ADMM-Reg) to the standard EM (1 subset), regularized SPS (SPS-Reg), NEG-ML and regularized NEG-ML (NEG-ML-Reg) algorithms. We used uniform image for the initial $\boldsymbol{x}$. For comparison, we also report evaluation results of our proposed method with the modified constraint $\boldsymbol{Ax} + \bar{\boldsymbol{r}}/2 \geqslant 0$. Changing the constraint requires a slight modification in (37):

$$v_i^{(n+1)} = [\hat{v}_i + \frac{\bar{r}_i}{2}]_+ - \frac{\bar{r}_i}{2}. \tag{59}$$

We exclude regularized EM in the comparison because regularized SPS and regularized EM converge to the same point.

In the plots shown in following subsections, β for regularization is 2^{-3} which is a value considering both the quantification in lesion and the benefit in noise. Van Slambrouck *et al* (2015) reported that ψ value near the mean counts in the sinogram increases the bias, therefore, ψ value should be large enough for bias-free reconstruction. We report the evaluation result of NEG-ML with $\psi = 4$ in the plots, however, section 4.3 enumerates all evaluation results with varying ψ and β values.

4.1. Evaluation result on 3D PET emulation

This section reports the evaluation results when a simulation replicates patient B condition and uses 168 projection angles. Figure 3 shows the results with plots showing how activity/contrast recovery versus iterations in VOIs evolve with iterations. Figure 3 also includes a plot of noise versus iterations.

NEG-ML without regularization achieves higher activity/contrast recovery in VOIs than regularized methods, however, it keeps increasing the noise with the iterations. This is undesirable because the algorithm needs to stop before convergence to have an acceptable noise level. Proposed algorithm gives higher activity/contrast recovery than other regularized algorithms, however, NEG-ML-Reg has lower noise in liver and FOV bias.

4.2. Result on fully 3D PET emulation

We also emulate the fully 3D (TOF) PET by increasing the number of projection angles (from 168 to 1680) for the same Patient B conditions of section 4.1. The results shown in figure 4 indicate that the converged evaluation results of NEG-ML-Reg (magenta) were changed compared to figure 3 (activity recovery in liver: 91.2% → 82.4%, contrast recovery in hot spot: 82.9% → 54.3%) while other algorithms including our proposed method remain similar.

Table 2. Comparison between regularized algorithms at the 400th iterations. We calculate the evaluation metrics using the results from 10 realizations.

Condition	β	NPA	Algorithm		ARL	CRH	CRC	FOVB	IEN
Patient A	2^{-3}	168	SPS-Reg		92.5	91.3	85.9	15.7	39.2
			NEG-ML-Reg	$\psi = 4$	94.8	91.2	94.6	**− 0.9**	**38.8**
				$\psi = 10^{-3}$	**96.2**	91.5	**95.3**	−11.5	41.2
			ADMM-Reg	$\boldsymbol{Ax} + \bar{\boldsymbol{r}}/2 \geqslant 0$	95.4	**91.9**	94.6	−7.1	39.9
				$\boldsymbol{Ax} + \bar{\boldsymbol{r}} \geqslant 0$	**96.2**	91.7	**95.3**	−14.1	41.5
		1680	SPS-Reg		92.6	91.3	86.1	15.8	38.9
			NEG-ML-Reg	$\psi = 4$	90.7	80.0	84.1	**0.0**	**12.1**
				$\psi = 10^{-3}$	96.1	91.6	95.8	−11.4	40.9
			ADMM-Reg	$\boldsymbol{Ax} + \bar{\boldsymbol{r}}/2 \geqslant 0$	95.5	91.6	**96.3**	−7.0	41.5
				$\boldsymbol{Ax} + \bar{\boldsymbol{r}} \geqslant 0$	**96.4**	**91.7**	96.0	−15.3	41.6
	2^{-6}	168	SPS-Reg		92.8	95.4	85.4	16.8	62.7
			NEG-ML-Reg	$\psi = 4$	96.5	95.9	97.9	**− 1.0**	80.7
				$\psi = 10^{-3}$	**97.6**	**96.4**	**98.6**	−11.4	82.8
			ADMM-Reg	$\boldsymbol{Ax} + \bar{\boldsymbol{r}}/2 \geqslant 0$	96.0	95.8	97.2	−2.3	**65.4**
				$\boldsymbol{Ax} + \bar{\boldsymbol{r}} \geqslant 0$	97.5	96.1	98.5	−13.7	80.6
		1680	SPS-Reg		92.9	95.6	85.7	16.9	62.3
			NEG-ML-Reg	$\psi = 4$	95.5	92.1	95.1	**0.0**	**38.5**
				$\psi = 10^{-3}$	97.7	96.5	99.1	−11.4	82.3
			ADMM-Reg	$\boldsymbol{Ax} + \bar{\boldsymbol{r}}/2 \geqslant 0$	96.5	96.5	100.6	−2.0	113.7
				$\boldsymbol{Ax} + \bar{\boldsymbol{r}} \geqslant 0$	**98.3**	**96.6**	**100.1**	−17.5	114.9
Patient B	2^{-3}	168	SPS-Reg		86.4	85.5	81.5	71.2	38.4
			NEG-ML-Reg	$\psi = 4$	91.2	82.9	84.7	**− 0.1**	**26.1**
				$\psi = 10^{-3}$	94.2	87.0	90.5	−60.3	40.4
			ADMM-Reg	$\boldsymbol{Ax} + \bar{\boldsymbol{r}}/2 \geqslant 0$	93.1	86.9	**91.3**	−37.2	40.5
				$\boldsymbol{Ax} + \bar{\boldsymbol{r}} \geqslant 0$	**94.3**	**87.1**	90.7	−67.4	40.6
		1680	SPS-Reg		86.4	85.7	80.9	70.8	38.0
			NEG-ML-Reg	$\psi = 4$	82.4	54.3	59.4	**− 0.7**	**6.2**
				$\psi = 10^{-3}$	94.2	87.2	89.2	−62.9	39.9
			ADMM-Reg	$\boldsymbol{Ax} + \bar{\boldsymbol{r}}/2 \geqslant 0$	93.0	87.1	**90.0**	−37.4	39.9
				$\boldsymbol{Ax} + \bar{\boldsymbol{r}} \geqslant 0$	**94.4**	**87.3**	89.3	−72.1	40.0
	2^{-6}	168	SPS-Reg		86.1	92.5	81.2	81.5	81.6
			NEG-ML-Reg	$\psi = 4$	96.1	92.6	93.7	**− 0.1**	**79.7**
				$\psi = 10^{-3}$	97.0	94.9	96.7	−64.6	108.9
			ADMM-Reg	$\boldsymbol{Ax} + \bar{\boldsymbol{r}}/2 \geqslant 0$	92.7	94.3	**99.0**	−10.1	117.6
				$\boldsymbol{Ax} + \bar{\boldsymbol{r}} \geqslant 0$	**97.1**	**95.1**	98.1	−88.4	122.8
		1680	SPS-Reg		85.9	92.7	79.9	81.0	81.0
			NEG-ML-Reg	$\psi = 4$	90.6	81.3	82.2	**− 0.6**	**22.5**
				$\psi = 10^{-3}$	97.0	95.1	94.8	−67.9	107.8
			ADMM-Reg	$\boldsymbol{Ax} + \bar{\boldsymbol{r}}/2 \geqslant 0$	92.5	94.5	**97.1**	−9.2	119.4
				$\boldsymbol{Ax} + \bar{\boldsymbol{r}} \geqslant 0$	**97.5**	**95.5**	96.3	−99.9	122.3

NPA: Number of Projection Angles, ARL: Activity Recovery in Liver.
CRH: Contrast Recovery in Hot spot, CRC: Contrast Recovery in Cold spot.
FOVB: FOV Bias, IEN: Image Ensemble Noise.

Figure 5 compares the images reconstructed using regularized algorithms when the number of projection angles changes (First row: 168, Second row: 1680). SPS-Reg and proposed algorithm (ADMM-Reg) generate almost identical images in two cases, however, the image from NEG-ML-Reg becomes blurry when the number of projection angles increases. The mean sinogram count decreased when we increased the number of projection angles so NEG-ML-Reg must make more approximations when calculating $\max(\psi, \bar{y}_i^{(n)})$ in (46). Therefore, the impact of parameter ψ on reconstruction depends on the count level of sinogram, implying that a parameter ψ value optimized at a certain count level could generate an unexpected result whenever there is a change in the amount of administered activity, radionuclide or detector geometry.

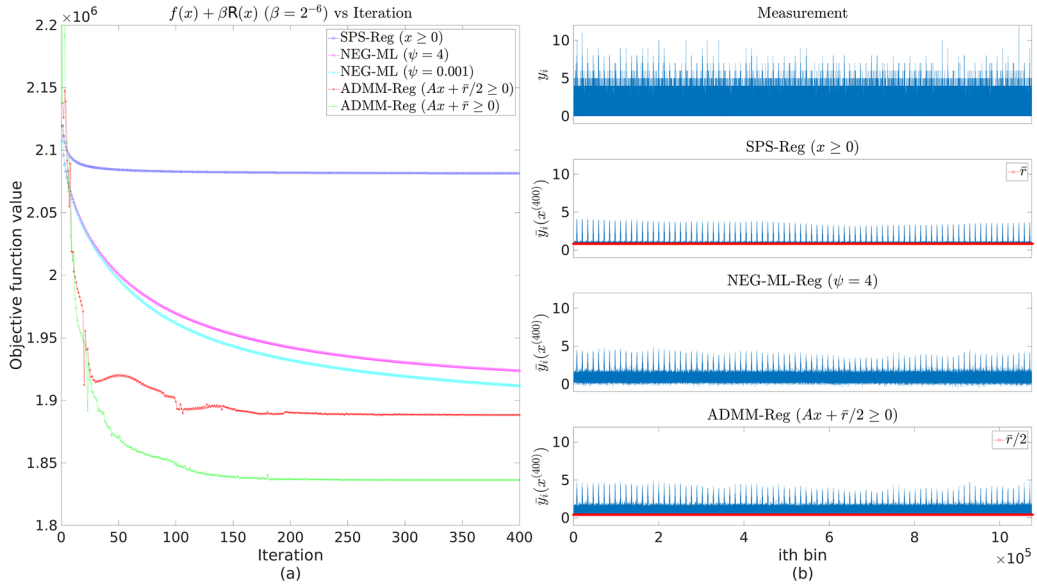

Figure 6. (a) Cost function value versus iteration. Proposed method with the constraint $\boldsymbol{Ax} + \bar{\boldsymbol{r}} \geqslant 0$ achieves the lowest cost function. (b) Measurement and estimated measurements. Standard method with conventional constraint (SPS-Reg) always predicts $\bar{y}_i(\boldsymbol{x})$ above $\bar{\boldsymbol{r}}$. Our proposed method finds $\hat{\boldsymbol{x}}$ within the larger set that satisfies the constraint (e.g. $\boldsymbol{Ax} + \bar{\boldsymbol{r}}/2 \geqslant 0$) rather than the conventional set ($\boldsymbol{x} \geqslant 0$).

4.3. Effect of algorithm parameter

We compare regularized algorithms by evaluating the reconstructed images at the 400th iteration in Table 2. Table 2 summarizes how changing β value for regularization, projection angles, ψ value for NEG-ML-Reg, random coincidence fraction and total true coincidence counts affects the reconstruction outputs. We also report evaluation results of our proposed method with the constraint $\boldsymbol{Ax} + \bar{\boldsymbol{r}} \geqslant 0$.

Better quantification result in Patient A case compared to Patient B case corresponds to the general knowledge that higher true coincidence counts and lower random coincidence fractions help to estimate the image precisely. We can also observe that higher β value for regularization decreases the noise, however, it worsens the other VOI metrics.

The algorithms that allow negative values in image domain (NEG-ML-Reg, ADMM-Reg) generally give better quantification result than the standard algorithm (SPS-Reg). A trend found in NEG-ML-Reg results is that lower ψ value leads to higher activity/contrast recovery. However, at the same time, FOV bias also increases. Moreover, increasing the number of projection angles always decreases the activity/contrast recovery of NEG-ML-Reg while SPS-Reg and our method (ADMM-Reg) remain fairly stable. This finding agrees with the results shown in the previous subsections. The constraint $\boldsymbol{Ax} + \bar{\boldsymbol{r}} \geqslant 0$ of our proposed method (ADMM-Reg) generally gives better quantification than $\boldsymbol{Ax} + \bar{\boldsymbol{r}}/2 \geqslant 0$ except FOV bias. $\boldsymbol{Ax} + \bar{\boldsymbol{r}} \geqslant 0$ gives 1–5% improvement in VOI metrics except FOV bias compared to $\boldsymbol{Ax} + \bar{\boldsymbol{r}}/2 \geqslant 0$, however, $\boldsymbol{Ax} + \bar{\boldsymbol{r}}/2 \geqslant 0$ reduces FOV bias significantly in Patient B case.

5. Discussion

As shown in the previous section, a main advantage of proposed algorithm is that we retain the original Poisson log-likelihood so there is no parameter that must be manually optimized. Choosing a number of iterations in $\boldsymbol{x}$-update for one ADMM iteration is an algorithm parameter. We chose 1 iterations in $\boldsymbol{x}$-update for one ADMM iteration. We can assign any value to ρ and the algorithm adapts its value automatically as explained in section 2.2.3. However, NEG-ML-Reg has a data-fit term parameter ψ that affects the results significantly and the optimal ψ value is different for each imaging condition. The NEG-ML-Reg algorithm can potentially be modified to automatically adapt the parameter ψ (i.e. multiplying some constant to the mean sinogram value), but any modification will need theoretical and experimental grounds beyond the scope of this paper. Nonetheless, setting ψ to very small value (i.e. $\psi = 10^{-3}$) makes NEG-ML-Reg robust to any count level as shown in the table 2. In this case, we observed that NEG-ML-Reg generates similar quantification in VOIs with proposed algorithm. However, NEG-ML-Reg with very small ψ gives high FOV bias and the algorithm does not have a room for modification to mitigate the FOV bias whereas our proposed method can reduce the FOV bias by slightly modifying the constraint (e.g. $\boldsymbol{Ax} + \bar{\boldsymbol{r}} \geqslant 0 \rightarrow \boldsymbol{Ax} + \bar{\boldsymbol{r}}/2 \geqslant 0$) without greatly impairing the other evaluation metrics.

Figure 6(a) shows how cost function value (40) of each method decreases with iterations when we simulate the measurement with patient B condition and 168 projection angles. Because NEG-ML-Reg solves the minimization of modified cost function (14) problem, our proposed method (ADMM-Reg) and NEG-ML-Reg converge to the different cost function value. Our proposed method (ADMM-Reg) with the constraint $\boldsymbol{Ax} + \bar{\boldsymbol{r}} \geqslant 0$ achieves the lowest cost function value. Figure 6(b) shows the measurement $\boldsymbol{y}$ (first row) and estimated measurements $\bar{\boldsymbol{y}}(\boldsymbol{x}^{(n)})$ at 400th iteration. The SPS-Reg estimate is always above $\bar{\boldsymbol{r}}$ because of the nonnegativity of system matrix element a_{ij} and the nonnegative constraint in image domain. Because NEG-ML-Reg does not enforce any constraint, $\bar{\boldsymbol{y}}(\boldsymbol{x}^{(400)})$ of NEG-ML-Reg has many negative valued predicted sinogram values. Lastly, we can check that estimates from our proposed method with constraint $\boldsymbol{Ax} + \bar{\boldsymbol{r}}/2 \geqslant 0$ lie above $\bar{\boldsymbol{r}}/2$. This confirms that our proposed method finds $\hat{\boldsymbol{x}}$ within the larger set that satisfies $\boldsymbol{Ax} + \bar{\boldsymbol{r}}/2 \geqslant 0$ rather than the conventional set ($\boldsymbol{x} \geqslant 0$).

A drawback of the proposed algorithm is that it requires more computation cost compared to the standard method and NEG-ML(-Reg) because of the need to compute matrix multiplication in (30) as well as auxiliary and dual variable. With our computer (Intel Core i7, 32 GB memory), 400 iterations of NEG-ML-Reg required 661 seconds for 168 projection views whereas proposed algorithm took 1116 seconds. Finding an acceleration method with a convergence guarantee is a future work topic.

6. Conclusion

This paper has presented a new PET reconstruction formulation with a relaxed nonnegativity constraint. The experimental results show that the proposed method reduces the bias in VOI when the true coincidence count-rate is low and the random fraction is high. The key of the proposed algorithm is incorporating the new constraint and adopting ADMM as a solver. Lastly our proposed method is not limited to Y-90 PET but has application in other imaging situations with low true count rates and high random fractions such as ion beam therapy (Kurz *et al* 2015).

Acknowledgment

This work was supported by grant R01 EB022075, awarded by the National Institute of Biomedical Imaging and Bioengineering, National Institute of Health, US Department of Health and Human Services. We thank the reviewers for particularly helpful comments that greatly improved the paper.

ORCID iDs

Hongki Lim https://orcid.org/0000-0002-2764-3730
Yuni K Dewaraja https://orcid.org/0000-0002-3920-6925
Jeffrey A Fessler https://orcid.org/0000-0001-9998-3315

References

Boyd S, Parikh N, Chu E, Peleato B and Eckstein J 2010 Distributed optimization and statistical learning via the alternating direction method of multipliers *Found. Trends Mach. Learn.* **3** 1–122

Byrne C 1998 Iterative algorithms for deblurring and deconvolution with constraints *Inverse Prob.* **14** 1455–67

Carlier T, Willowson K P, Fourkal E, Bailey D L, Doss M and Conti M 2015 Y90-PET imaging: exploring limitations and accuracy under conditions of low counts and high random fraction *Med. Phys.* **42** 4295–309

De Pierro A R 1995 A modified expectation maximization algorithm for penalized likelihood estimation in emission tomography *IEEE Trans. Med. Imaging* **14** 132–7

Erdogan H and Fessler J A 1999 Monotonic algorithms for transmission tomography *IEEE Trans. Med. Imaging* **18** 801–14

Erlandsson K, Visvikis D, Waddington W, Cullum I, Jarritt P and Polowsky L 2000 Low-statistics reconstruction with AB-EMML *IEEE Nuclear Science Symp. Conf. Record* vol 2 (IEEE) pp 15–249

Fessler J A and Erdogan H 1998 A paraboloidal surrogates algorithm for convergent penalized-likelihood emission image reconstruction *Proc. IEEE Nuclear Science Symp. Medical Imaging Conf.* vol 2 pp 1132–5

Grezes-Besset L, Nuyts J, Boellard R, Buvat I, Michel C, Pierre C, Costes N and Reilhac A 2007 Simulation-based evaluation of NEG-ML iterative reconstruction of low count PET data *IEEE Nuclear Science Symp. Conf. Record* vol 4 (IEEE) 3009–14

Kurz C, Bauer J, Conti M, Guérin L, Eriksson L and Parodi K 2015 Investigating the limits of PET/CT imaging at very low true count rates and high random fractions in ion-beam therapy monitoring *Med. Phys.* **42** 3979–91

Li S Z 1998 Close-form solution and parameter selection for convex minimization-based edge-preserving smoothing *IEEE Trans. Pattern Anal. Mach. Intell.* **20** 916–32

Nuyts J, Stroobants S, Dupont P, Vleugels S, Flamen P and Mortelmans L A dedicated ML-algorithm for non-attenuation corrected PET whole body images *Proc. IEEE Nuclear Science Symp. Medical Imaging Conf.* vol 2, pp 13–6

Nuyts J, Stute S, Van Slambrouck K, van Velden F, Boellaard R and Comtat C 2011 Maximum-likelihood reconstruction based on a modified poisson distribution to reduce bias in PET *IEEE Nuclear Science Symp. Conf. Record*

Pasciak A S, Bourgeois A C, McKinney J M, Chang T T, Osborne D R, Acuff S N and Bradley Y C 2014 Radioembolization and the dynamic role of 90Y PET/CT *Frontiers Oncol.* **4** 38

Pasciak A S, McKinney J M and Bradley Y C 2016 *Handbook of Radioembolization: Physics, Biology, Nuclear Medicine and Imaging* (Boca Raton, FL: CRC Press)

Sotthivirat S and Fessler J A 2002 Image recovery using partitioned-separable paraboloidal surrogate coordinate ascent algorithms *IEEE Trans. Im. Proc.* 11 306–17

Strydhorst J, Carlier T, Dieudonné A, Conti M and Buvat I 2016 A GATE evaluation of the sources of error in quantitative 90Y PET *Med. Phys.* **43** 5320–9

Van Slambrouck K, Stute S, Comtat C, Sibomana M, van Velden F, Boellaard R and Nuyts J 2015 Bias reduction for low-statistics PET: maximum likelihood reconstruction with a modified Poisson distribution *IEEE Trans. Med. Imaging* **34** 126–36

Willowson K P, Tapner M and Bailey D L 2015 A multicentre comparison of quantitative 90Y PET/CT for dosimetric purposes after radioembolization with resin microspheres *Eur. J. Nucl. Med.* **42** 1202–22